

# Geometrically Thick Disks around Kerr Black Holes in a Swirling Universe

Kristian Gjorgjieski\*

*Department of Physics, Carl von Ossietzky University of Oldenburg, 26111 Oldenburg, Germany*

Rogério Capobianco†

*Instituto de Física de São Carlos, Universidade de São Paulo, São Carlos, São Paulo 13560-970, Brazil*

(Dated: May 28, 2024)

We investigate geometrically thick disks around Kerr black holes in a swirling universe. This stationary and axisymmetric spacetime is composed of a Kerr black hole, which is immersed in a swirling background. The swirling background is characterized by an odd  $\mathcal{Z}_2$  symmetry, where the northern and southern hemispheres are rotating in opposite directions. The Kerr and swirling rotations can lead to the emergence of complex spin-spin interactions, which heavily influence the spacetime properties. In order to study this influence, we analyze prograde as well as retrograde circular orbits and geometrically thick disks for different spacetime solutions, which are classified by their Kerr parameter  $a$  and the swirling parameter  $j$ . We find stabilizing effects on prograde circular orbits and destabilizing effects on retrograde circular orbits, which originate from the spin-spin interaction and depend mainly on the Kerr rotation. Furthermore, the background rotation leads to an emergence of static orbits and the symmetry breaking regarding the equatorial plane causes a vertical distribution of the circular orbits and thick torus solutions. Due to the destabilizing effect of the swirling rotation, an outer marginally stable orbit appears, which heavily downsizes the parameter space for disk solutions. Dependent on the Keplerian specific angular momentum distribution of the spacetime and on the disk momentum  $\ell_0$ , different types of disk are possible which we classify and which differ in terms of the complex disk dynamics that could arise due to the presence of an inner and outer cusp or just an outer cusp.

## 1. INTRODUCTION

Accretion disks are structured accumulations of matter around astrophysical compact objects. Diffuse matter gets attracted by the central object and settles in circular orbits. The formed large-scale structure resembles a disk or a torus. In complex disk interactions, angular momentum gets exchanged from the inner to the outer regions of the disk, which causes matter to migrate from the outside inwards through the disk to smaller and smaller orbits towards the central object. When the matter reaches the marginally stable orbit, small perturbations could lead to an inspiral of the matter and it ultimately gets accreted by the central object. The energy converted in this process scales with the mass of the central object and in the example of supermassive black holes, it corresponds to magnitudes that can be found at the upper end of our current energy scales for observed and theorized phenomena in the universe. Accretion disks are therefore particularly important in the study of high-energy physics and in the observation of astrophysical objects, as a large part of the energy is converted into radiation energy, with such high intensities, that it can be observed from billions of light years away. This radiation can have a broad frequency spectrum, which mainly depends on the disk properties and the properties of the central object. Disregarding various subclasses, accretion disks can generally be divided into slim and thick disks. In this paper we will focus on the class of thick accretion disks, which was first introduced in the 70s [1–5] and profoundly analyzed in the 80s [6–10].

The simplest case of a thick disk imposes the *Polish Doughnut* model, where the disk is modeled as a non-selfgravitating perfect fluid and where its properties are solely determined by the spacetime geometry. Due to its simplicity, this approach offers analytical solutions that are directly computed from the metric components. Nevertheless, these solutions capture qualitatively the main properties of possible disks and are therefore often used as initial conditions in more complex GRMHD simulations [11–13]. Polish Doughnuts have been studied for a variety of alternative gravity and compact object solutions [14–21]. Recently Polish Doughnuts around a Schwarzschild black hole in a swirling universe were analyzed [22], where the Swirling background gives rise to unique features like an outer disk cusp. In this work, we will focus on geometrically thick tori around Kerr black holes in a swirling universe and study their properties.

---

\* kristian.gjorgjieski@uol.de

† rogerio.capobianco@gmail.com

In general, the swirling universe describes a rotating spacetime, which is not asymptotically flat. The formalism to obtain a swirling universe solution originates from the works of Frederick J. Ernst, who proposed in 1968 a method to obtain new solutions from the Einstein field equations for stationary and axisymmetric (electro-)vacuum spacetimes [23, 24]. In this formulation, the field equations, which are in general a system of coupled non-linear differential equations, are replaced by the *Ernst equations*. The Ernst equations are composed of two coupled partial differential equations for a complex gravitational and electromagnetic potential. Since these equations are integrable, they can be solved by a set of solution generating techniques, which can furthermore be applied to build new solutions from Einstein's field equations by using the invariance of the Ernst potentials under some set of transformations. Recently, compositions of these transformations have been used to generate new solutions [25]. In particular, the swirling universe is obtained by the application of Ehlers transformation to a Minkowski seed solution and was first presented in [26]. It was rediscovered in [27], which in addition to the reintroduction of the background solution, also immersed Schwarzschild and Kerr black holes in the swirling universe, in a similar fashion like Ernst immersed black holes into magnetic universes [28]. The swirling spacetime is characterized by the swirling parameter  $j$ , which is responsible for the addition of exotic features to the seed solution, such as the appearance of an ergoregion that extends to infinity, in the presence or absence of compact objects. A detailed description of that ergoregion and the geodesic motion in the swirling universe can be found in [29]. The swirling spacetime is stationary, axisymmetric, and harbours an odd  $\mathcal{Z}_2$  symmetry, where the background frame dragging changes its sign in the lower hemisphere (with respect to the equatorial plane). As a consequence, the spacetime in the lower hemisphere rotates in the opposite direction as in the upper hemisphere. The spacetime of a Schwarzschild black hole immersed in this swirling universe (SBHSU) is fully characterized by the mass of the black hole and by the swirling parameter of the spacetime. The spacetime of a Kerr black hole immersed in a swirling universe (KBHSU), is fully characterized by the black hole mass, the Kerr parameter, and the swirling parameter. The KBHSU is co-rotating with the swirling background in one hemisphere and counter-rotating in the other since the Kerr parameter does not change its sign with respect to the equatorial plane. This breaking of symmetry and the spin-spin interaction of the Kerr rotation with the swirling rotation has an influence on the main properties of the spacetime, like the ergoregions, as well as the circular orbits and accretion tori solutions, which are usually symmetrical with respect to the equatorial plane. The main goal of this work is to analyze these properties, how they are affected by the swirling parameter for different Kerr parameters, and how they change with variation of the swirling and Kerr parameters.

The structure of this work is as follows: In section 2 we introduce the KBHSU solution and briefly discuss its main properties. In section 3 a introduction to the theory of geometrically thick accretion disks is presented, and in section 4 we analyze qualitatively the circular orbits and thick disk solutions of the KBHSU spacetime. Throughout this work we use the Einstein convention and geometrized units, where  $G = c = 1$ , with  $G$  as the gravitational constant and  $c$  as the speed of light. The metric signature used is  $(-, +, +, +)$  and in all KBHSU solutions throughout this work, the mass of the KBHSU is normalized to  $M = 1$ .

## 2. KERR BLACK HOLE IN A SWIRLING UNIVERSE

The line element describing a Kerr black hole immersed in a swirling universe can be written in Boyer-Lindquist coordinates as [27]

$$ds^2 = \frac{1}{\mathcal{F}(r, \theta)} (d\varphi + \omega dt)^2 + \mathcal{F}(r, \theta) \left[ -\rho^2 dt^2 + \Sigma \sin^2 \theta \left( \frac{dr^2}{\Delta} + d\theta^2 \right) \right], \quad (1)$$

where the metric functions  $\mathcal{F}$  and  $\omega$ , that encode the swirling parameter  $j$ , can be expressed in a finite power series in the form of

$$\mathcal{F} = \frac{\mathcal{F}_0 + j\mathcal{F}_1 + j^2\mathcal{F}_2}{R^2 \Sigma \sin^2 \theta} \quad ; \quad \omega = \frac{\omega_0 + j\omega_1 + j^2\omega_2}{\Sigma}, \quad (2)$$

with

$$\begin{aligned} \mathcal{F}_0 &= R^4, & \mathcal{F}_1 &= 4am\Xi \cos \theta R^2, & \mathcal{F}_2 &= 4a^2 m^2 \Xi^2 \cos^2 \theta + \Sigma^2 \sin^4 \theta \\ \omega_0 &= 2amr, & \omega_1 &= 4 \cos \theta (ma^4 - r^4(r - 2m) - \Delta a^2 r - a(r - m)\Omega), \\ \omega_2 &= 2m [3ar^5 - a^5(r + 2m) + 2a^3 r^2(r + 3m) - r^3(\cos^2 \theta - 6)\Omega + a^2 \Omega (\cos^2 \theta (3r - 2m) - 6(r - m))], \end{aligned}$$

where

$$\begin{aligned}\Delta &= r^2 - 2mr + a^2, & \rho^2 &= \Delta \sin^2 \theta, & \Sigma &= (r^2 + a^2)^2 - \Delta a^2 \sin^2 \theta, \\ \Omega &= \Delta a \cos^2 \theta, & \Xi &= r^2 (\cos^2 \theta - 3) - a^2 (1 + \cos^2 \theta), & R^2 &= r^2 + a^2 \cos^2 \theta.\end{aligned}$$

The pure Kerr solution is recovered for vanishing  $j$ , the immersion of Schwarzschild in a swirling universe is obtained by  $a = 0$ , and the pure swirling universe is found for  $m = 0$  and  $a = 0$ . As noted in [27] the spin-spin interaction between the Kerr black hole and the background dragging gives rise to a conical singularity on the symmetry axes. Furthermore, the KBHSU solution possesses two horizon surfaces, an inner and an outer one, which in these coordinates are found by imposing  $g^{rr} = 0$ , and thus are defined by

$$r_{\pm} = m \pm \sqrt{m^2 - a^2}, \quad (3)$$

which is independent of  $j$  and equivalent to the Kerr solution. However, it should be noted, that the presence of the background dragging will deform the horizon geometry. Considering the main interest of this paper, we will focus only on the outer horizon here. Taking a slice of constant  $t$  leads to the induced metric

$$ds_{hor}^2 = \Sigma(r_{\pm}, \theta) \sin^2 \theta \mathcal{F}(r_{\pm}, \theta) d\theta^2 + \frac{d\varphi^2}{\mathcal{F}(r_{\pm}, \theta)}. \quad (4)$$

Insights about the shape of the horizon can be taken by considering an isometric embedding of the two-dimensional surface (4) into a three-dimensional Euclidean space. However, a full embedding is typically not always possible. For the pure Kerr solution, i.e.  $j = 0$ , the event horizon geometry around the poles becomes hyperbolic as the Kerr parameter increases ( $a \in (\sqrt{3}/2, 1)$ ) and thus an embedding of those regions into a Euclidean space is not feasible. For that case, insights about the geometry can be shown by considering the composition of a Euclidean embedding with the metric  $ds_E^2 = dx^2 + dy^2 + dz^2$  and a pseudo-Euclidean embedding with metric  $ds_{pE}^2 = dx^2 + dy^2 - dz^2$  [30, 31].

The presence of the swirling background affects the north and south hemispheres differently, which is also directly reflected in the horizon geometry. We note that even small variations of  $j$  deform the usual oblate structure of the Kerr horizon. For a positive spin-spin relation ( $aj > 0$ ) the neighborhood of  $(r = r_+, \theta = \pi)$  becomes hyperbolic. For a rapidly rotating Kerr black hole, where the neighborhood of the poles is already hyperbolic, the vicinity of  $(r = r_+, \theta = 0)$  is dragged into an elliptic geometry. In Fig. 1 we show a representation of the outer horizon for a variation of the swirling parameter,  $j \in \{0, 10^{-4}, 10^{-3}\}$ , and two values of the Kerr parameter,  $a \in \{0.5, 0.9\}$ . For a negative spin-spin relation ( $aj < 0$ ) an analogous behaviour would be observed, where just the northern and southern hemispheres are interchanged.

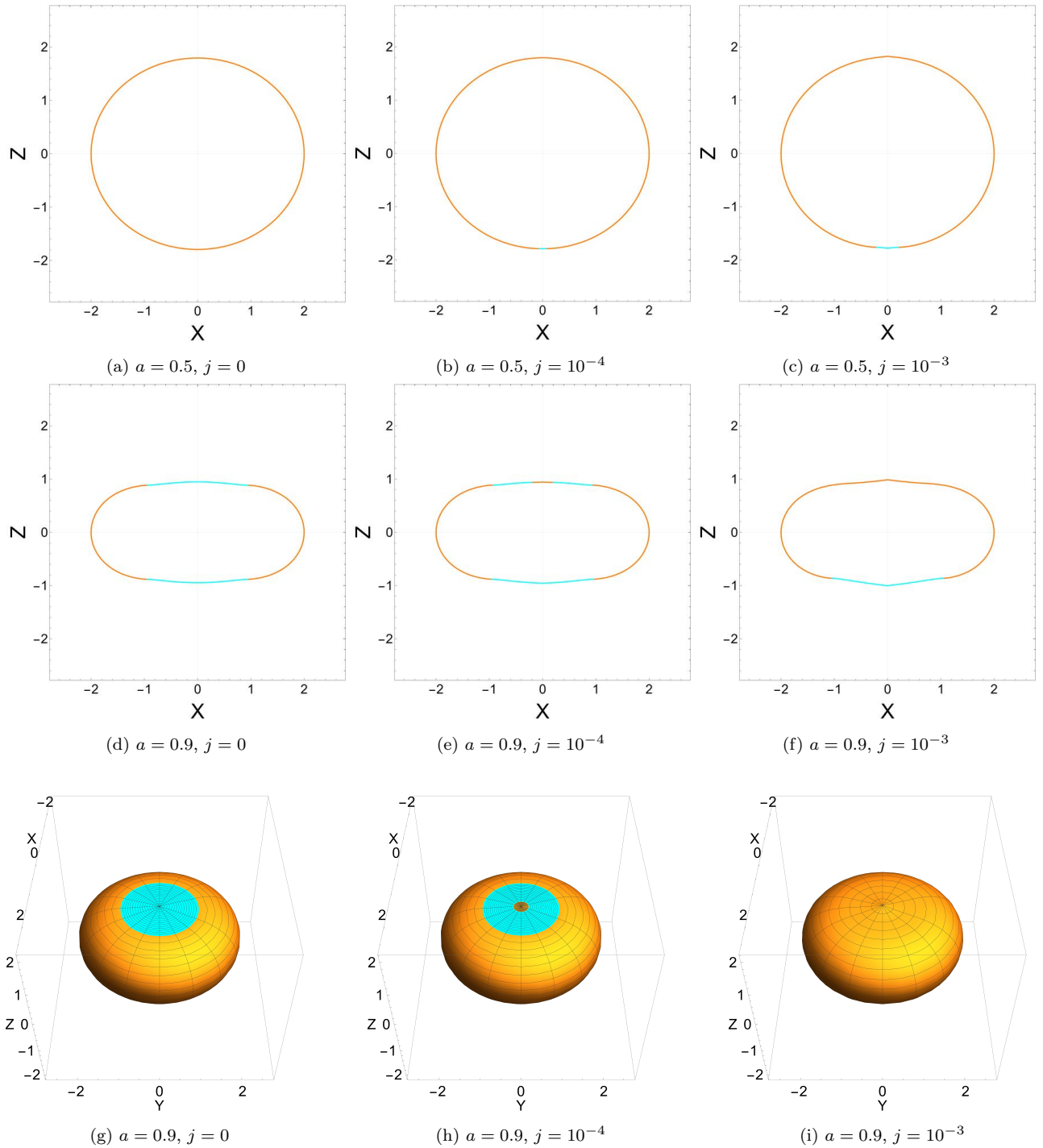


Fig. 1: Embeddings of the outer horizon geometry for different KBHSU solutions and small variations of the swirling parameter  $j$ . The orange curves and surfaces represent an Euclidean embedding, the cyan curves and surfaces represent a pseudo-Euclidean embedding. The top row shows the horizon geometry for a KBHSU with Kerr parameter  $a = 0.5$ , where the vicinity of the southern pole becomes hyperbolic due to the swirling dragging. This effect increases with  $j$ . The middle row shows the geometry for a rapidly rotating KBHSU with  $a = 0.9$ . Here, the regions close to the northern and southern poles are already hyperbolic and with increasing  $j$  the horizon region close to the northern pole becomes elliptic. The bottom row presents a 3D representation of the embedding for the rapidly rotating case with  $a = 0.9$ . The equatorial plane has been set to be  $Z(\pi/2) = 0$  in all plots.

When  $j$  increases further, the geometry of the event horizon is significantly modified. Some examples are shown in Fig. 2, where we have chosen the limiting Kerr parameter  $a = \sqrt{3}/2$  to illustrate the hyperbolic behaviour appearing



due to the swirling dragging.

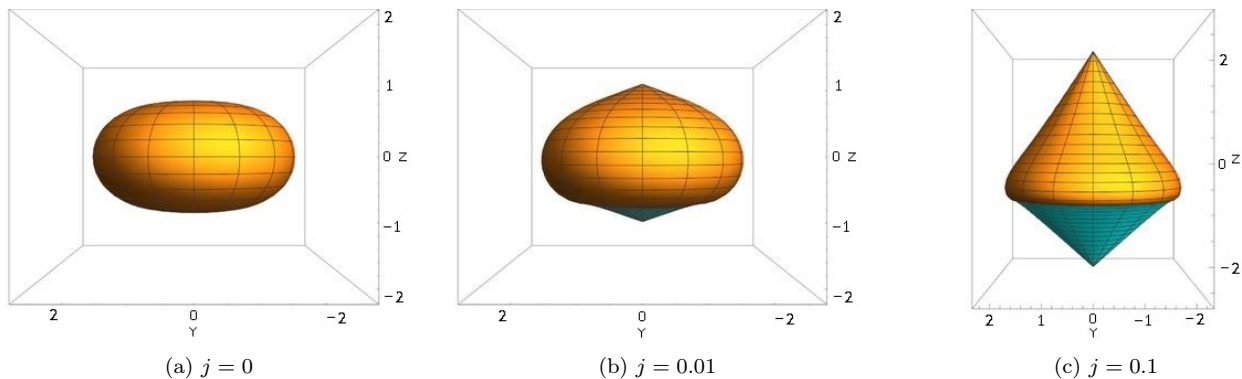


Fig. 2: Embedding of the outer horizon geometry for a fixed value of  $a = \sqrt{3}/2$  and three values of the swirling parameter,  $j \in \{0, 0.01, 0.1\}$ . The equatorial plane is set to  $Z(\pi/2) = 0$ . With increasing  $j$  the horizon geometry becomes more conical and the symmetry breaking between the northern and southern hemispheres is more accentuated. A large part of the horizon geometry in the southern hemisphere becomes hyperbolic for larger values of  $j$ .

Despite the significant changes in geometry, the horizon area is not affected by the presence of the swirling parameter  $j$ ,

$$\mathcal{A} = \int_0^{2\pi} \int_0^\pi \sqrt{g_{\theta\theta}g_{\varphi\varphi}} d\theta d\varphi = \int_0^{2\pi} \int_0^\pi \sqrt{\sin^2 \theta \Sigma} d\theta d\varphi \Big|_{r=r_\pm} = 8m\pi r_\pm, \quad (5)$$

which has already been seen for the Schwarzschild black hole in a swirling universe [27? ].

The ergosurfaces for the KBHSU solution are rather complicated and change significantly depending on  $j$ . Since it appears not to be possible to find simple analytical relations, as it is possible for pure Kerr and the swirling universe background, we perform a qualitative study on the boundaries of the ergoregions, which are defined by the condition  $g_{tt} = 0$ . The pure Kerr solution has two of these ergosurfaces, an inner and an outer closed surface that touches the respective horizons on the symmetry axis, thus

$$r_{E_-}(m, a, \theta) \leq r_- < r_+ \leq r_{E_+}(m, a, \theta), \quad (6)$$

where  $r_{E_\pm}$  is the radial coordinate of the inner and outer ergosurface, respectively. These surfaces are also present in the KBHSU solution and the constraints given in Eq. 6 still hold for the KBHSU case. Furthermore, two additional ergosurfaces appear, which for small values of  $j$  are disconnected patches in the southern and northern hemispheres extending to infinity. These surfaces are a property of the swirling background. They appear also for the Schwarzschild black hole immersed in a swirling universe. A detailed discussion of these ergosurfaces can be found in [27, 29? ]. For the main interest of this paper, we will restrict the discussion of the ergoregions to the outer area, i.e.  $r > r_+$ .

The ergoregions of the KBHSU are intrinsically related to the spin-spin interaction of black hole and swirling background. For smaller variations of  $j$ , the ergosurfaces resemble roughly a superposition of the intrinsic ergoregions from each spacetime (Kerr and swirling universe) described above. This is illustrated in Fig. 3 below. In Fig 4 we show a representation of these surfaces in a three-dimensional space for a small value of  $j = 0.01$ .

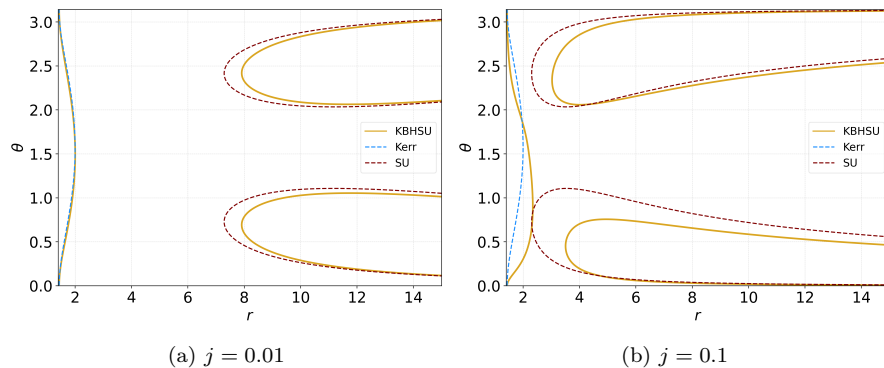


Fig. 3: Comparison of the ergosurfaces for KBHSU, Kerr, and the swirling universe (SU) in the  $r - \theta$  plane for two different values of the swirling parameter. The orange curves show the outer KBHSU ergosurfaces, the blue dashed curve shows the outer Kerr ergosurface, and the red dashed curves show the swirling universe ergosurfaces. The Kerr parameter is set to a  $a = 0.9$  in both plots.

The KBHSU ergosurface, which corresponds to the outer Kerr surface remains qualitatively similar for small values of  $j$  (Fig. 3 (a)). The ergosurfaces originating from the swirling background show a minor deviation for smaller  $j$ , but their general structure is similar. However, as  $j$  increases, the ergosurfaces deviate more and more from the Kerr and swirling universe surfaces and are not just a combination of these any longer. The non-linear spin-spin interaction causes greater symmetry breaking for larger  $j$  and the ergosurfaces become more asymmetrical with respect to the equatorial plane.

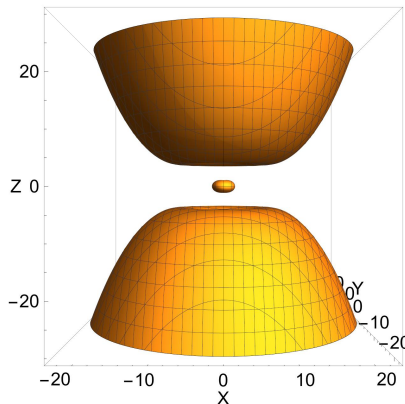


Fig. 4: Representation of the outer KBHSU surfaces in a three-dimensional space with  $Z(\pi/2) = 0$ . The Kerr parameter is set to  $a = 0.9$  and the swirling parameter to  $j = 0.01$ . The inner structure showcases the ergosurface which originates from the outer Kerr surface and the structures in the northern and southern hemispheres showcase the ergosurfaces, which originate from the swirling universe ergosurfaces. This representation is obtained by considering the rotation around the symmetry axis.

Generally, we conclude, that the spin-spin interaction between the black hole and the swirling background enhances the symmetry breaking regarding the spacetime properties, as showcased for the horizons and ergosurfaces. This symmetry breaking also has an influence on the properties of circular orbits and thick disks as we will showcase in the following sections. For further reading on the general properties of the KBHSU spacetime, we can point out, that a more detailed discussion is in development.

### 3. GEOMETRICALLY THICK DISKS

In axisymmetric and stationary spacetimes geometrically thick disks can be modeled as a body of fluids, where the fluid particles are moving on circular orbits around a central compact object. The stress-energy tensor of the disk,

$T^{\mu\nu}$ , can be written as a sum of the different contributing terms, i.e. the fluid, viscosity, radiation, and magnetic terms. In general, the degree of complexity of the model can increase significantly if the various terms are taken into account. In the Polish doughnut model, the viscosity, radiation, and magnetic terms are neglected, and only the fluid part is taken into account. The accretion disk is therefore modeled as a perfect fluid and due to its simplicity, it offers a suitable model to investigate the qualitative properties of geometrically thick accretion disks. The stress-energy tensor in the Polish doughnut model is given by

$$T^{\mu\nu} = T_{Fluid}^{\mu\nu} = \rho h u^\mu u^\nu + p g^{\mu\nu}, \quad (7)$$

where  $\rho$  is the rest-mass density,  $h$  is the specific enthalpy,  $u^\mu = (u^t, 0, 0, u^\varphi)$  is the four-velocity of the fluid particles,  $p$  is the pressure and  $g^{\mu\nu}$  is the contra-variant metric tensor. To construct disk solutions the fundamental conservation laws, i.e. the conservation of energy-momentum and the continuity equation need to be solved,

$$\nabla_\mu T^{\mu\nu} = 0 \quad (8)$$

$$\nabla_\mu (\rho u^\mu) = 0. \quad (9)$$

The continuity equation (9) is always trivially satisfied, since  $u^r = u^\theta = 0$  for circular motion and  $\partial_t = \partial_\varphi = 0$  due to the axisymmetry and stationarity of the spacetime. By applying the orthogonal projection tensor  $h^\alpha_\beta = \delta^\alpha_\beta + u^\alpha u_\beta$  in eq. (8) and rewriting it in terms of the specific angular momentum  $\ell$  and the angular velocity  $\Omega$ , the relativistic Euler equations can be derived,

$$\partial_\mu (\ln |u_t|) - \frac{\Omega}{1 - \Omega\ell} \partial_\mu \ell = -\frac{1}{\rho h} \partial_\mu p, \quad (10)$$

where  $-u_t$  is the mass-normalized energy. As a necessary integrability condition the von Zeipel theorem must be assumed, which states that the angular velocity can be written as a function of the specific angular momentum,  $\Omega = \Omega(\ell)$ . By assuming a polytropic equation of state, where the pressure is solely a function of the density, such as  $p = K\rho^\Gamma$ , with  $K$ ,  $\Gamma$  constant, the von Zeipel theorem is satisfied. Hence, the eq. (10) becomes integrable and can be written as

$$\ln |u_t| - \ln |(u_t)_{in}| - \int_{\ell_{in}}^{\ell} \frac{\Omega}{1 - \Omega\ell'} d\ell' = - \int_{p_{in}}^p \frac{dp'}{\rho h} = - \int_{h_{in}}^h \frac{dh'}{h'} = - \ln h, \quad (11)$$

where the subscript *in* refers to the inner edge of the accretion disk. Assuming a uniform specific angular momentum distribution of the disk, the integral term regarding the specific angular momentum vanishes and the right-hand side can be defined as an effective potential,  $\mathcal{W} = \ln |u_t|$ ,  $\mathcal{W}_{in} = \ln |(u_t)_{in}|$ , which corresponds to the combined gravitational and centrifugal potential. The effective potential at the inner edge of the disk,  $\mathcal{W}_{in}$ , is taken as a free parameter. In order to represent all physically feasible solutions, it will be set to  $\mathcal{W}_{in} = 0$  in all further calculations. Rewriting the specific enthalpy in eq. (11) in terms of the rest-mass density is leading to,

$$\mathcal{W} - \mathcal{W}_{in} = \ln \left( 1 + \frac{K\Gamma\rho^{\Gamma-1}}{\Gamma - 1} \right). \quad (12)$$

The rest-mass density can therefore be expressed as a function of the effective potential  $\mathcal{W}$ . As a consequence, the equi-density and equi-pressure surfaces coincide with the equi-potential surfaces. Since  $\partial_\mu \mathcal{W} = 0$  is satisfied for  $a_\mu = 0$ , the motion at the local extrema of the effective potential is geodesic. Furthermore, the pressure gradient vanishes at the local extrema of the effective potential. Minima of  $\mathcal{W}$  correspond to maxima of the pressure and therefore indicate a disk center (stable geodesic motion of the fluid particles). Maxima of  $\mathcal{W}$  corresponds to the minima of the pressure and mark disk cusps (unstable geodesic motion of the fluid particles). The effective potential  $\mathcal{W}$  can be expressed through the metric components and the specific angular momentum as,

$$\mathcal{W} = \frac{1}{2} \ln \left( \frac{g_{t\varphi}^2 - g_{tt}g_{\varphi\varphi}}{\ell^2 g_{tt} + 2g_{t\varphi}\ell + g_{\varphi\varphi}} \right). \quad (13)$$

Due to the odd  $\mathcal{Z}2$  spacetime symmetry in the KBHSU solution, the local extrema of the potential are not located in the equatorial plane for  $j \neq 0$ . In order to determine the locations of the extrema, one needs to solve therefore the system of equations composed of  $\partial_r \mathcal{W} = 0$  and  $\partial_\theta \mathcal{W} = 0$  for the specific angular momentum  $\ell$ . The resulting distribution of  $\ell$ , which solves this system of equations, represents therefore the Keplerian specific angular momentum  $\ell_K$  of the circular geodesics in that spacetime. For a chosen specific angular momentum  $\ell_0$  of the disk, the location of the disk center is then given by  $(r_{center}, \theta_{center}) = \{(r, \theta) : \ell_K(r, \theta) = \ell_0 \wedge \partial_r \ell_K(r, \theta) > 0\}$  and of a disk cusp by  $(r_{cusp}, \theta_{cusp}) = \{(r, \theta) : \ell_K(r, \theta) = \ell_0 \wedge \partial_r \ell_K(r, \theta) < 0\}$ .

#### 4. CIRCULAR ORBITS AND DISK SOLUTIONS

In order to conduct an exemplary study of circular orbits and geometrically thick disks around KBHSU, we have analyzed different solutions, which are classified by their Kerr spin parameter  $a$ . For a representative analysis regarding the Kerr spin parameter range, we selected solutions in the lower, middle and upper parameter range, namely  $a = 0.2$ ,  $a = 0.5$  and  $a = 0.9$ . To investigate the influence of the swirling parameter  $j$  on the solutions, we have varied  $j$  for the mentioned Kerr spin parameters and analyzed the resulting spacetime and disk properties. The swirling parameter  $j$  was thereby set to  $j \in \{0, 10^{-5}, 10^{-4}, 2 \cdot 10^{-4}, 5 \cdot 10^{-4}\}$ . The Fig. 5 illustrates the specific angular momentum of circular orbits for the different Kerr spin parameters and varying swirling parameters.

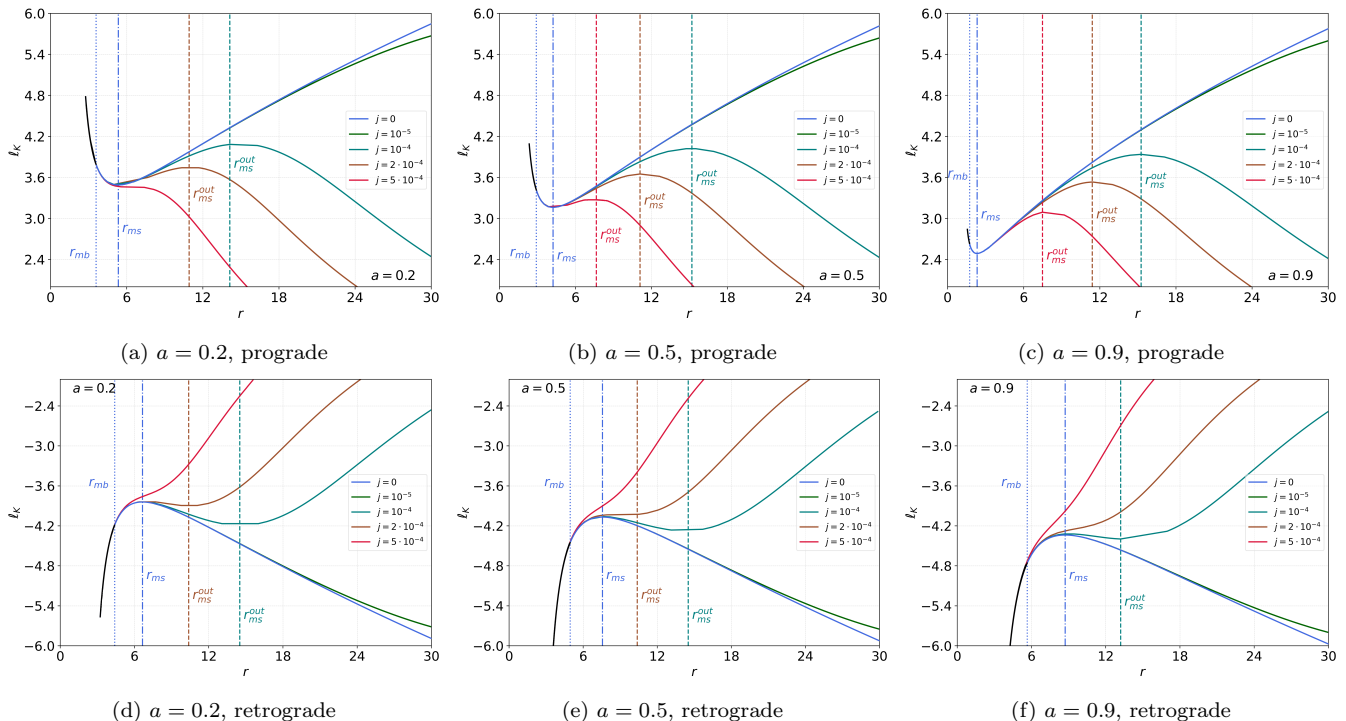


Fig. 5: Specific angular momentum  $\ell_K$  of circular orbits for the different Kerr parameter solutions with varying swirling parameter  $j$ . The upper row presents  $\ell_K$  for prograde orbits and the lower row presents  $\ell_K$  for retrograde orbits. The terms prograde and retrograde refer here to the rotation direction of the KBHSU, which is defined by the Kerr spin parameter  $a$ . The dotted vertical line in each plot marks the marginally bound orbit  $r_{mb}$  and the dashed-dotted vertical line marks the marginally stable orbit  $r_{ms}$  of the Kerr solution ( $j = 0$ ). Dashed vertical lines mark the outer marginally stable orbits  $r_{ms}^{out}$ , which appear for the KBHSU solutions ( $j \neq 0$ ). Black curve sections mark unbound orbits.

The specific angular momentum of circular orbits changes significantly for the KBHSU solutions compared to the Kerr solutions. Up to a critical value of the swirling parameter,  $j_c$ , the specific angular momentum develops an outer extremum. For prograde orbits this extremum is a maximum, for retrograde orbits it is a minimum (Fig. 5 upper and lower row). For radial values beyond the outer extremum, the specific angular momentum converges asymptotically to 0 in both cases. The outer extremum corresponds to the emergence of an outer marginally stable orbit for KBHSU solutions. Stable circular orbits are therefore only possible in a specific spacetime region, which is lower bounded by the inner marginally stable orbit and upper bounded by the outer marginally stable orbit. The inner marginally stable orbits of the KBHSU solutions are closely located to the marginally stable orbit of the Kerr solution. A greater deviation of  $\ell_K$  from the Kerr solution is only noticeable from the inner extremum outwards. For solutions with a swirling parameter greater than the critical swirling parameter,  $j > j_c$ , the extrema vanishes and the specific angular momentum becomes monotonic, all circular orbits are therefore unstable. For prograde orbits this critical value  $j_c$  increases with increasing Kerr spin parameter  $a$ , therefore stable circular orbits are possible for a larger range of the swirling parameter  $j$  (Fig. 5 upper row). For retrograde orbits the value of  $j_c$  decreases with increasing Kerr spin parameter  $a$ , stable circular orbits for fast rotating KBHSU occur therefore for a smaller range of the swirling parameter (Fig. 5 lower row). The swirling rotation causes furthermore the emergence of static orbits for prograde as well as retrograde motion. An illustration of the rest specific angular momentum, which is used to determine the

static orbits, can be found in Fig. 6.

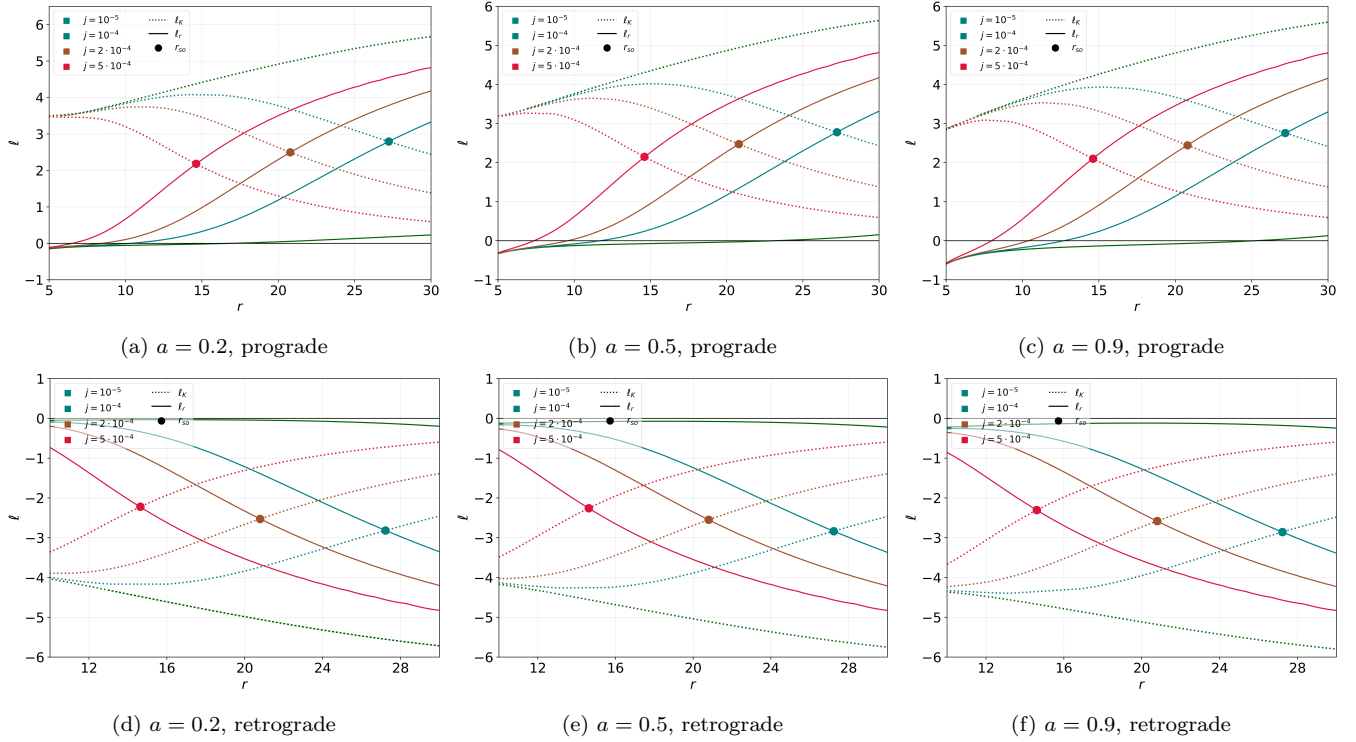


Fig. 6: Rest specific angular momentum,  $\ell_r = -\frac{gt_\varphi}{g_{tt}}$ , plotted alongside the prograde and retrograde circular orbits for the various KBHSU solutions. The previously shown  $\ell_K$  distributions are plotted as dotted curves for comparison. The circular marker symbols indicate the radial location of the static orbits,  $r_{so}$ . At these radial locations  $\ell_K$  is identical to  $\ell_r$  and as a consequence, the corresponding circular orbit is a static orbit.

The rest specific angular momentum  $\ell_r$  alongside the circular orbits has an intersection with  $\ell_K$  for the analyzed KBHSU solutions. The specific angular momentum of the circular orbit corresponding to this intersection is equal to the specific angular momentum a particle at rest would have in the co-moving reference frame. Therefore a test particle, which is initially at rest in the co-moving reference frame, would always stay at rest in this reference frame in the absence of disturbances. However, it should be noted that all static orbits are unstable since the intersection point for each solution is outwards of  $r_{ms}^{out}$ . Furthermore, for  $r > r_{so}$  the absolute value of  $\ell_K$  is smaller than  $\ell_r$  for prograde as well as retrograde motion. Thus, all circular orbits outwards of the static orbit are counter-rotating in the co-moving reference frame of the spacetime background. With increasing  $j$  the radial location  $r_{so}$  of the static orbits is moving inwards, regardless of the Kerr parameter  $a$ . The differences between the various Kerr parameters are in general negligible,  $r_{so}$  is located for each solution roughly at the same radial location for a fixed  $j$ , regardless of the rotational direction. Therefore we conclude, that the Kerr parameter and rotation direction have a lesser impact on the properties of static orbits, which are mostly determined by  $j$ .

As mentioned in section 3, the circular geodesics are not located in the equatorial plane, in contrast to the Kerr solution. To each point of the presented curves for the  $\ell_K$  and  $\ell_r$  distributions, there is a corresponding varying  $\theta$  coordinate. For a better understanding regarding the spatial distribution of the circular orbits, a cross-section plot is depicted in Fig. 7 for the various analyzed KBHSU solutions.

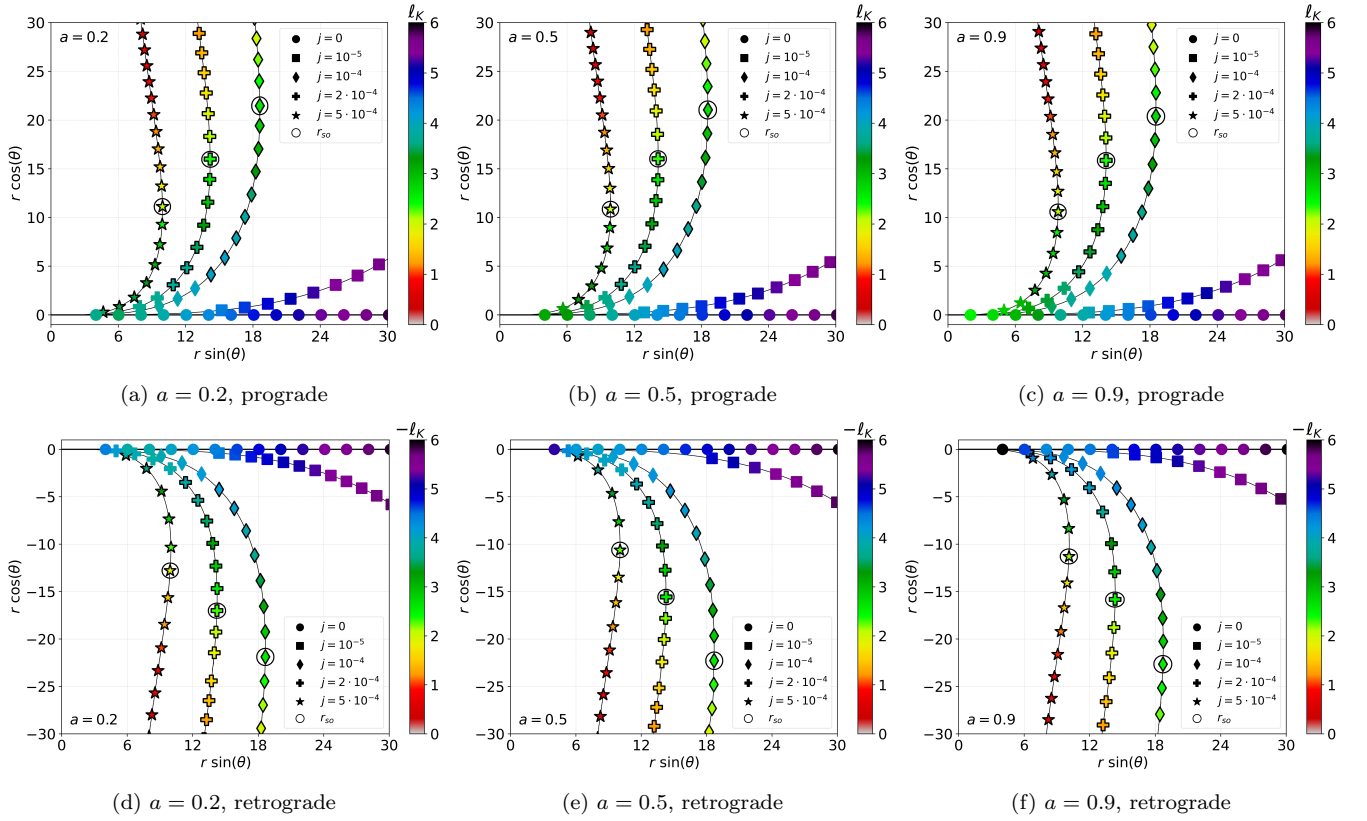


Fig. 7: Cross section plots of circular orbits and their corresponding specific angular momentum  $\ell_K$  for the different Kerr parameter solutions with varying swirling parameter  $j$ . The upper row presents  $\ell_K$  of prograde orbits and the lower row presents  $\ell_K$  for retrograde orbits. The terms prograde and retrograde refer here to the rotation direction of the KBHSU, which is defined by the Kerr spin parameter  $a$ . The different symbols mark selected solutions for circular orbits for varying  $j$ . They are coloured according to their specific angular momentum, which is described by the scale on the right of each plot. Unstable orbits are marked by a black edge around the symbol and the static orbits are marked by a circle.

The spatial location of KBHSU circular orbits is highly affected by the swirling parameter, it deviates from the equatorial plane and is located in planes orthogonal to the rotational axis in the upper and lower hemispheres. With increasing  $j$  the verticality of the circular orbit distribution increases and for  $\ell_K \rightarrow 0$  the height of the corresponding circular orbit above or below the equatorial plane diverges. The location of the static orbits is largely unaffected by  $a$  and for increasing  $j$  it moves closer to the equatorial plane. Stable orbits are only possible close to the equatorial plane. In the case of prograde motion, the orbits are solely located in the upper hemisphere (Fig. 7 upper row), they are therefore co-moving with the swirling background. For retrograde motion, the orbits are solely located in the lower hemisphere (Fig. 7 lower row). Since the frame-dragging direction of the swirling background changes its sign for the lower hemisphere, a counter-rotating test particle regarding the Kerr rotation is co-moving with the swirling background in the lower hemisphere. All circular orbits are therefore co-moving with their surrounding spacetime background reference frame. The spatial distribution of circular orbits throughout the Kerr parameter range is very similar, the influence of the Kerr parameter is negligible. We conclude, that the general properties of circular orbits for KBHSU are largely determined by the swirling parameter, with the Kerr parameter playing a minor role. However, the Kerr parameter has a significant influence on the angular momentum distribution and the stability of the circular orbits. The rotation of the KBHSU has a stabilizing effect on the co-rotating orbits and a destabilizing effect on the counter-rotating orbits. This can be attributed to the rotation of the swirling background. Orbits located in the lower-hemisphere are co-rotating with the spacetime background but counter-rotating with the black hole, which is inducing instabilities due to the opposite spin direction of the swirling and Kerr rotation. The magnitude of this effect grows with increasing swirling and Kerr parameters  $j$  and  $a$ .

As a consequence accretion disks with an uniform constant angular momentum can exist only for a specific range of  $\ell_0$ , which is lower bounded by  $\ell_{ms}^{in}$  and upper bounded by  $\ell_{ms}^{out}$ , since only for  $\ell_0 \in [\ell_{ms}^{in}, \ell_{ms}^{out}]$  stable circular orbits exist. Thus, disk solutions with static orbits and static surfaces do not exist. The disk center can only be located between  $r_{ms}^{in}$  and  $r_{ms}^{out}$  and with increasing  $j$  the solution space for prograde accretion tori gets smaller, as the solution

range of stable orbits decreases. Due to the stabilizing effect of the KBHSU rotation, the solution space for prograde (retrograde) accretion tori is greater (smaller) for faster rotating KBHSUs compared to slower rotating ones. This is depicted exemplarily in Fig. 8 for  $j = 10^{-4}$  and varying values for  $\ell_0$ .

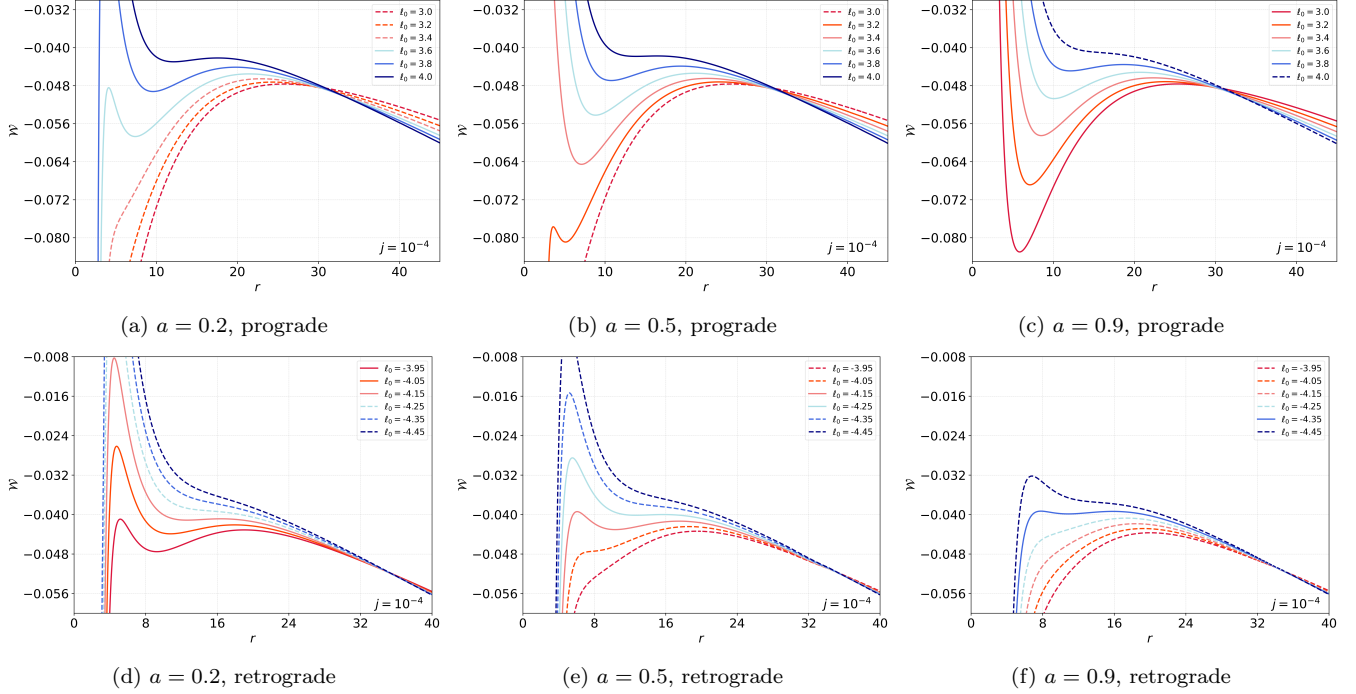


Fig. 8: Effective potential  $\mathcal{W}$  alongside circular orbits for the different Kerr spin parameters and various  $\ell_0$ . The swirling parameter is set to  $j = 10^{-4}$  in all solutions. The upper row presents  $\mathcal{W}$  for prograde motion and the lower row for retrograde motion (referring to the rotation direction defined by the Kerr parameter  $a$ ). Dashed curves indicate solutions for which no disks can exist, due to the absence of a local minimum.

With increasing  $a$  prograde disk exists for a greater range of  $\ell_0$  for the same  $j$  (Fig. 8 upper row). For retrograde disks, the solution space narrows down for the same  $j$  and  $\ell_0$  parameter range (Fig. 8 lower row). All possible disk solutions can be classified into two main types: Type 1 solutions are composed of an inner cusp and an outer cusp, between which the disk center is located. The inner cusp corresponds to an inner local maximum, the disk center to the local minimum and the outer cusp to the outer local maximum of the effective potential  $\mathcal{W}$ . These solutions can be further classified into three subtypes: Type 1a disks, where the inner maximum is greater than the outer maximum (e. g. Fig. 8 (d)). Type 1b disks, where the outer maximum is greater than the inner maximum (e. g. Fig. 8 (b)). And the special case Type 1c, where the inner and outer potential maxima have the same value. It can be viewed as the limiting case of a Type 1a or 1b solution. In contrast to Type 1 solutions, Type 2 solutions are only composed of a disk center and an outer cusp, the effective potential has therefore one minimum and only one maximum, located to the outside of the minimum (e. g. Fig. 8 (c)). With increasing  $a$  the disk solution space moves from mostly Type 1 solutions to Type 2 solutions for prograde disks. For retrograde disks all solutions are of Type I. Exemplary cross-section plots of the different disk types are presented in Fig. 9 for prograde disks. In the case of retrograde disk, the defined disk types are analogous, besides that only solutions of Type 1 exist.



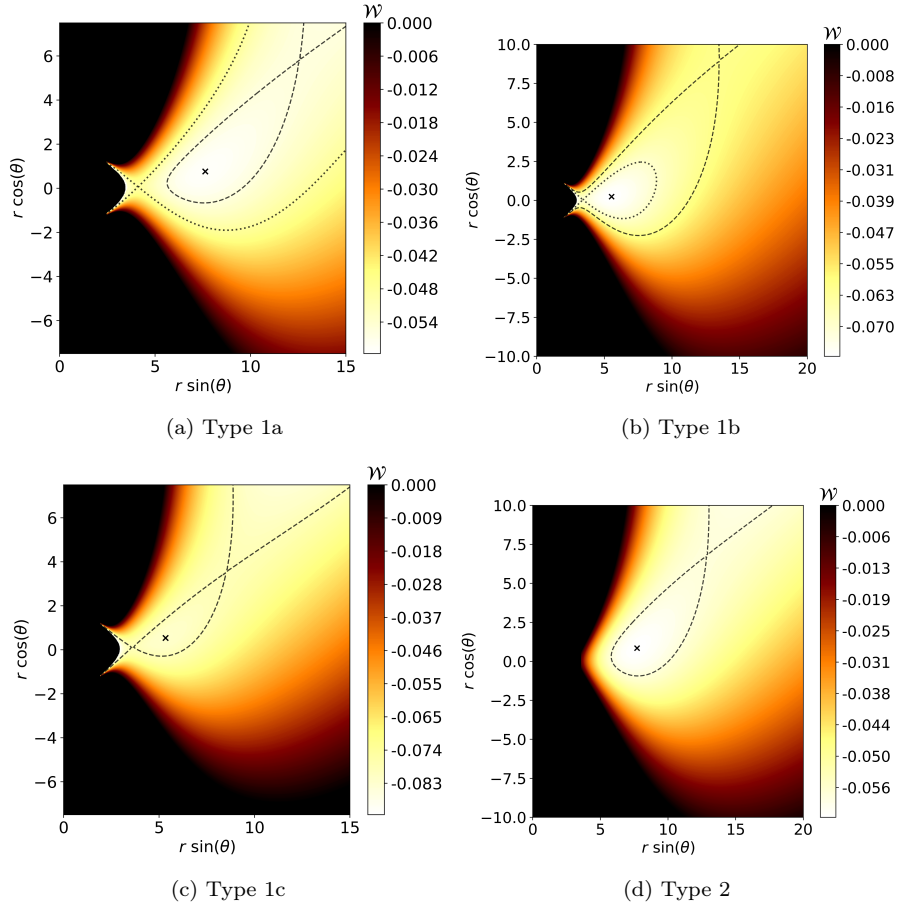


Fig. 9: Meridional cross section of  $\mathcal{W}$  for the different disk types. As an example for a Type 1a disk, the parameters  $a = 0.2$ ,  $j = 2 \cdot 10^{-4}$  and  $\ell_0 = 3.6$  where used. For Type 1b the parameters  $a = 0.5$ ,  $j = 2 \cdot 10^{-4}$  and  $\ell_0 = 3.23$ . For Type 1c the parameters  $a = 0.5$ ,  $j = 5 \cdot 10^{-4}$  and  $\ell_0 = 3.1964$  and for Type 2 the parameters  $a = 0.5$ ,  $j = 2 \cdot 10^{-4}$  and  $\ell_0 = 3.45$ . The dotted curve corresponds to the equi-potential surface of the inner cusp, the dashed curve corresponds to the equi-potential surface of the outer cusp. The  $\times$  symbol marks the location of the disk center.

For Type 1a disks the equi-potential surface of the inner cusp is not closed, it is open towards the KBHSU center and expands from the cusp outwards to infinity. The equi-potential surface of the outer cusp is semi-closed, with the closed region containing the disk center and the open region expanding from the outer cusp towards infinity. This enclosed region with the disk center is fully surrounded by the equi-potential surface of the inner cusp. Depending on the initial conditions various disk evolutions seem possible, as the complexity of disk dynamics could increase due to the presence of two cusps. Matter could be accreted through the inner cusp by flowing past the center region, without having a major effect on the dynamics and stability of the center region, as it is fully enclosed by the equi-potential surface of the outer cusp. On a different note, the whole disk could become unstable, since matter from the disk center could disperse through the outer cusp to unstable orbits, leading to a diffusion of the whole inner disk region. In case of Type 1b disks, the equi-potential surface of the inner cusp is semi-closed, it fully encloses the disk center and is open towards the KBHSU center. The equi-potential surface of the outer cusp is open towards the KBHSU center and from the outer cusp outwards to infinity. It surrounds the inner cusp potential surface and the disk center. Accretion processes through both cusps are conceivable. Matter from outside could accrete through the outer cusp towards the KBHSU center, flowing past the center region. Accretion from the disk center through the inner cusp towards the KBHSU could also take place. Since the center region is fully surrounded by the outer cusp potential surface, an indirect accretion process could take place, where matter flows through the outer cusp towards the inner potential surface, feeding the central region of the accretion disk, which could trigger an accretion process through the inner cusp. In the limiting case Type 1c, the effective potential at the inner and outer cusp is identical, the corresponding equi-potential surface has therefore two intersections and is open towards the KBHSU center and open outwards of the outer cusp. Between the inner and outer cusp it fully encloses the disk center region. An accretion process may happen through the outer cusp towards the disk center and through the inner cusp towards the KBSHU center. The



disk could also disperse if matter from the center region flows through the outer cusp to the outer regions. For Type 2 disks only an outer cusp exists, with the equi-potential surface of the cusp being closed towards the KBHSU and open outwards of the cusp towards infinity. As for Type 1a disks it fully encloses the disk center. Due to the absence of an inner cusp, no accretion processes without additional inner-physical disk effects are possible. Nevertheless, the discussed runaway instability for Type 1 disks could also apply to Type 2 disks, where matter dispersing through the outer cusp towards unstable orbits could lead to a diffusion of the center region.

In order to investigate the influence of the Kerr parameter on prograde disk properties, different exemplary solutions for the same parameters, besides the Kerr parameter, are presented in Fig. 10.

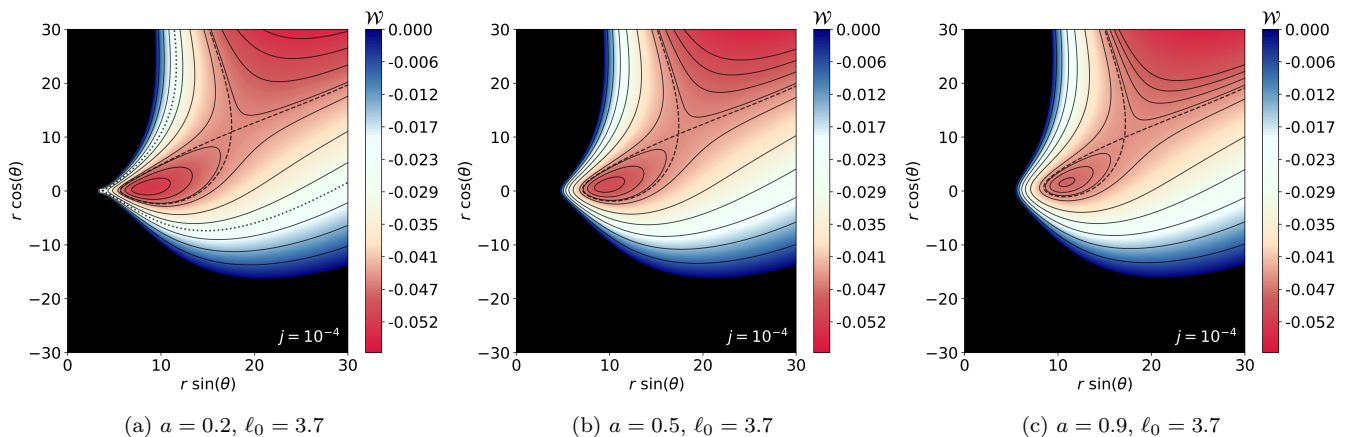


Fig. 10: Meridional cross section of the effective potential  $\mathcal{W}$  for different disk solutions with the same swirling parameter  $j = 10^{-4}$  and different Kerr parameter  $a$ . The specific angular momentum of the disks is set to  $\ell_0 = 3.7$  in all solutions. The lower boundary of the scale is set in all solutions to  $\mathcal{W} = -0.055$  for better comparison. Black curves represent equi-potential surfaces. The dotted curve in (a) corresponds to the equi-potential surface going through the inner cusp. Dashed curves represent the equi-potential surface going through the outer cusp.

Using the same disk parameters besides the Kerr parameter reveals, that prograde disk solutions are in their general morphology largely unaffected by the Kerr parameter. All disk solutions are asymmetrical to the equatorial plane and their spatial distribution is similar, regardless of the Kerr parameter. They extend mainly into the upper hemisphere with only a small region extending into the lower hemisphere. This effect originates from the  $\mathcal{Z}_2$  symmetry of the swirling background and increases with increasing  $j$ . We follow, that even in the vicinity of the KBHSU, the Kerr rotation gets dominated by the swirling rotation albeit  $j$  being small compared to  $a$ . However, differences regarding the physical disk properties are noticeable. For the same disk parameters, the effective potential for the slower Kerr rotation has a deeper minimum and therefore a higher density at the center of the disk compared to the faster rotation. The disk solution for  $a = 0.2$  is of Type 1a, where the disk center is enclosed by the equi-potential surface of the outer cusp, which itself is surrounded by the equi-potential surface of the inner cusp (Fig. 10 (a)). The  $a = 0.5$  and  $a = 0.9$  disk solutions are of Type 2, with only an outer cusp. Since they do not possess an inner cusp, no accretion process without further inner-physical disk effects is possible. For faster rotating KBHSUs, prograde disks solutions exist for higher  $j$  and for lower  $\ell_0$ , leading to more compact disks, as shown in Fig. 11.

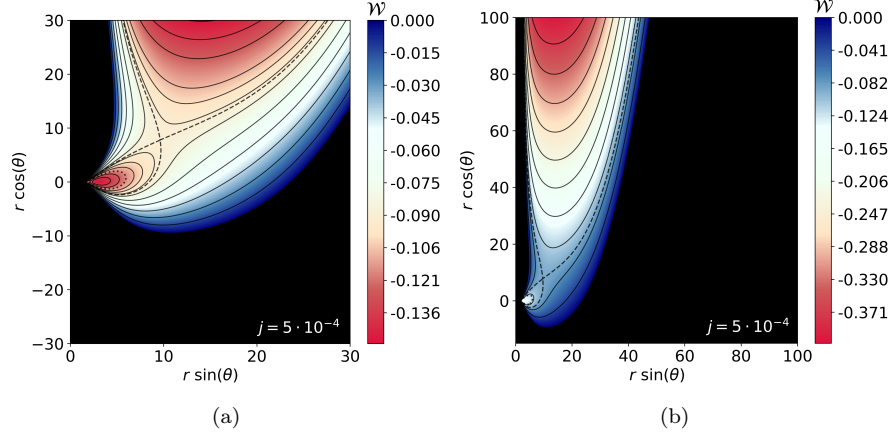


Fig. 11: Meridional cross section of the effective potential  $\mathcal{W}$  for a Type 1b disk with  $a = 0.9$ ,  $j = 5 \cdot 10^{-4}$  and  $\ell_0 = 2.55$ . (a) presents a more detailed view of the center region, with the dotted curve corresponding to the equi-potential surface of the inner cusp. (b) presents a broader view of the vertical structure. The dashed curves represent the equi-potential surface going through the outer cusp in both plots.

In this Type 1b solution, the center region is highly compact, most of the matter is located close the density maximum (minimum of  $\mathcal{W}$ ) and the disk center is located closely to the KBHSU center. The effective potential decreases monotonically outwards the outer cusp also on a greater scale. We follow, that with increasing  $a$  and  $j$  and decreasing  $\ell_0$  disk solutions are more localized and compact. The verticality of the disk structure is mainly affected by the swirling parameter. Since with increasing  $a$  disk solutions are possible for larger values of  $j$ , solutions with a greater verticality are possible for faster rotating KBSHU.

In the following Fig. 12 examples of retrograde disk solutions are presented for various values of  $a$ ,  $j$  and  $\ell_0$ . Due to the more limited disk solution space for retrograde disks, solutions with the same  $\ell_0$  and  $j$  value do not exist for the picked Kerr parameters ( $a \in \{0.2, 0.5, 0.9\}$ ). A comparison for different Kerr parameters but same swirling and disk parameters, like done for the prograde disks, is therefore not possible. Thus, we picked exemplary solutions with different parameters to showcase the main properties of retrograde disks.

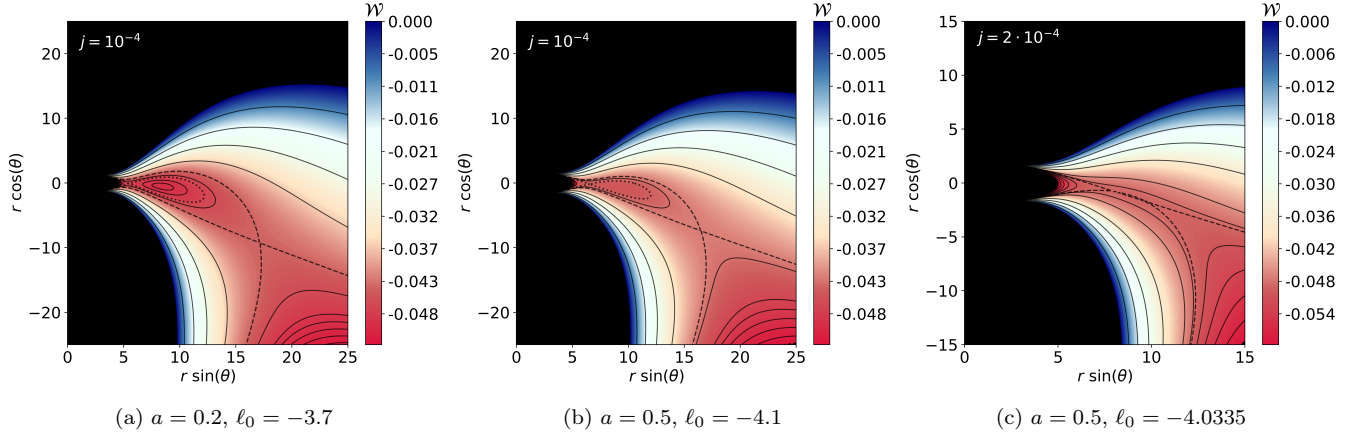


Fig. 12: Meridional cross section of the effective potential  $\mathcal{W}$  for different retrograde disk solutions. Black curves represent equi-potential surfaces. Dotted curves correspond to the equi-potential surface of the inner cusp. Dashed curves represent the equi-potential surface of the outer cusp.

Retrograde disks are similar to prograde disks regarding their asymmetry with reference to the equatorial plane. In contrast to prograde disks, they extend mainly into the lower hemisphere with only a small part extending into the upper hemisphere. This corresponds to the spatial distribution of the retrograde circular orbits, which originates from the change of the swirling rotation in the lower hemisphere, and with increasing  $j$  this asymmetry and verticality of the disk increases. The Figs. 12 (a) and (b) present retrograde Type 1b disks, for which the same properties apply as

explained for the prograde case. Fig. 12 (c) illustrates a retrograde Type 1c disk, where the effective potential at the inner and outer cusp has the same value. This value is also closely located to the potential minimum. The potential difference between the disk center and inner/outer cusp is miniscule, which causes the enclosed region between inner and outer cusp to appear as vanishing. The only stable region of the disk lies inside this small narrow region close to the disk center. Regarding disk dynamics this solution could therefore be highly unstable. The following Fig. 13 presents a retrograde disk solution for the fast rotating KBSHU with  $a = 0.9$ .

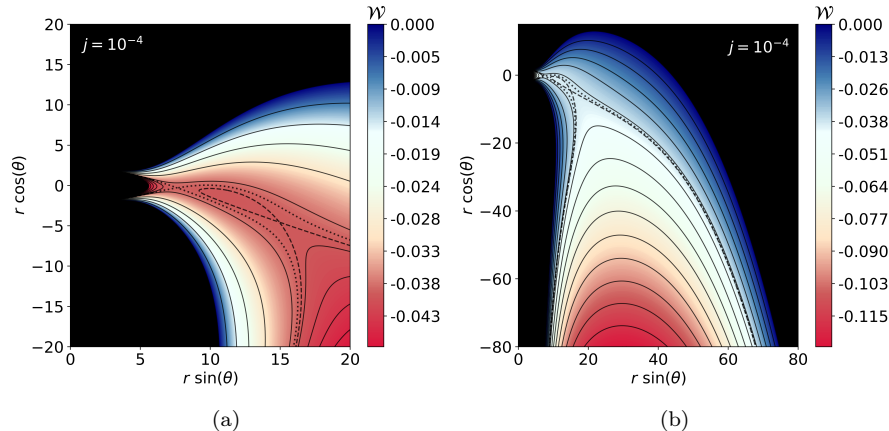


Fig. 13: Meridional cross section of the effective potential  $\mathcal{W}$  for a retrograde Type 1a disk with  $a = 0.9$ ,  $j = 10^{-4}$  and  $\ell_0 = -4.36$ . (a) presents a more detailed view of the center region, with the dotted curve corresponding to the equi-potential surface of the inner cusp. (b) presents a broader view of the vertical structure. The dashed curves represent the equi-potential surface going through the outer cusp in both plots.

This presented solution is of Type 1a, with the equi-potential surface of the outer cusp enclosing the disk center. The main disk properties are similar as explained for the prograde Type 1a disks. Nevertheless, for faster rotating KBSHU the retrograde disk center moves outwards and the disks are less compact compared to other disk solutions. This is also reflected by the large scale structure (Fig. 13 (b)), where the horizontal extension is greater compared to the prograde case for  $a = 0.9$ , due to the smaller swirling parameter  $j$ . A greater verticality would correlate with a higher value of the Swirling parameter, however the retrograde disk solution space regarding the Swirling parameter is very limited in case of faster rotating KBSHU, since for higher  $j$  no stable circular orbits and therefore no disk solutions exist.

## 5. CONCLUSION

In this work, we investigated qualitatively geometrically thick disks around Kerr black holes in a swirling universe. We classified different KBHSU solutions by their Kerr spin parameter  $a$  and varied for fixed  $a$  the swirling parameter  $j$ , to analyze the influence of the swirling background and the effects of the spin-spin interaction between black hole and background. For an exemplary analysis regarding the circular orbits and disk solutions, we chose the Kerr parameters  $a = 0.2$ ,  $a = 0.5$ , and  $a = 0.9$ , for slow, medium, and fast rotating black holes, respectively. The swirling parameter was varied between  $j = 10^{-5}$  and  $5 \cdot 10^{-4}$ , as for higher values of  $j$  no disk solutions exist. We analyzed prograde orbits and disks, as well as retrograde orbits and disks. In both cases, the properties of the orbits and disks are highly affected by the swirling parameter, as circular orbits deviate from the equatorial plane with increasing  $j$ . Prograde (retrograde) orbits get shifted into the upper (lower) hemisphere, where they are comoving with the swirling background and the verticality of the spatial distribution increases with  $j$  for all possible values of  $a$ . The differences regarding the spatial distribution for the different Kerr parameters are negligible. The Keplerian specific angular momentum distribution develops in all cases an additional outer extremum, which marks an outer marginally stable orbit. The range of stable orbits is therefore bounded by the inner and outer marginally stable orbit, which also severely limits the parameter range of possible disk solutions.

In the case of prograde orbits, we found a stabilizing effect of the spin-spin interaction, since for higher values of  $a$  stable circular orbits were possible for larger  $j$ . Faster rotating black holes harbour therefore a broader parameter space for prograde disk solutions. For retrograde orbits, which are all located in the lower hemisphere, we found the opposite effect. In the lower hemisphere, the black hole is counter-rotating to the swirling background, which has a

destabilizing effect on the circular orbits. Therefore with increasing  $a$  the range of stable circular orbits decreases for larger  $j$  and the parameter space for disk solutions shrinks.

In all solutions, the rotation of the swirling background causes the emergence of a static orbit at which a test particle is at rest in the co-moving reference frame. Since the rest specific angular momentum has a higher absolute value for all orbits outside the static orbit, test particles on these outside orbits are counter-rotating in the co-moving reference frame of spacetime.

Due to the outer extremum of the Keplerian specific angular momentum all possible disk solutions possess an outer cusp. In dependence of the spacetime solutions and the chosen value of the disk momentum  $\ell_0$  we found and classified four different possible disk types. Type 1 solutions are characterized by an inner cusp and an outer cusp, between which the disk center lies. Type 2 solutions only exist for prograde disks for the analyzed values of  $a$  and are characterized by the absence of an inner cusp, they only possess an outer cusp. The Type 1 solutions can be further subclassified regarding the potential values at the cusps. For Type 1a solutions, the effective potential has a higher value at the inner cusp than the outer cusp. This causes the equi-potential surfaces of the inner cusp to be open towards the center and towards the outer disk regions. The equi-potential surface of the outer cusp fully encloses the disk center region and is closed towards the KBHSU center but open towards the outer region. In the case of Type 1b solutions, the effective potential of the outer cusp has a higher value than the inner cusp. This causes the equi-potential surface of the outer cusp to be open towards the center and towards the outer region. The inner cusp potential surface now fully encloses the disk center, it is closed towards the outer region and open towards the KBHSU center. In the special case Type 1c the effective potential has the same value at the inner and outer cusp, the potential surface is fully closed between the inner and outer cusp and it encloses the disk center, but is open towards the KBHSU center and towards the outer disk region. All mentioned solutions have a high complexity of disk dynamics due to the different conceivable accretion mechanisms regarding the inner as well as the outer cusp. However, direct accretion onto the KBHSU, with the absence of inner-physical disk effects, is only possible for Type 1 solutions as Type 2 do not possess an inner cusp and are closed towards the KBHSU center.

#### ACKNOWLEDGMENTS

We would like to thank Betti Hartmann and Jutta Kunz for discussions. R.C. is grateful to CAPES for financial support under Grant No: 88887.371717/2019-00, and would like to thank the University of Oldenburg for hospitality.

- 
- [1] M. A. Abramowicz, The Relativistic von Zeipel's Theorem, *Acta Astronomica* **21**, 81 (1971).
  - [2] M. A. Abramowicz, Theory of Level Surfaces Inside Relativistic: Rotating Stars. II., *Acta Astronomica* **24**, 45 (1974).
  - [3] L. G. Fishbone and V. Moncrief, Relativistic fluid disks in orbit around Kerr black holes., *Astrophys. J.* **207**, 962 (1976).
  - [4] M. Abramowicz, M. Jaroszynski, and M. Sikora, Relativistic, accreting disks., *Astronomy and Astrophysics* **63**, 221 (1978).
  - [5] M. Kozłowski, M. Jaroszynski, and M. A. Abramowicz, The analytic theory of fluid disks orbiting the Kerr black hole., *Astronomy and Astrophysics* **63**, 209 (1978).
  - [6] M. A. Abramowicz, M. Calvani, and L. Nobili, Thick accretion disks with super-Eddington luminosities, *Astrophys. J.* **242**, 772 (1980).
  - [7] M. Jaroszynski, M. A. Abramowicz, and B. Paczynski, Supercritical accretion disks around black holes, *Acta Astronomica* **30**, 1 (1980).
  - [8] B. Paczyński and P. J. Wiita, Thick Accretion Disks and Supercritical Luminosities, *Astronomy and Astrophysics* **88**, 23 (1980).
  - [9] B. Paczynski and G. Bisnovatyi-Kogan, A Model of a Thin Accretion Disk around a Black Hole, *Acta Astronomica* **31**, 283 (1981).
  - [10] B. Paczynski and M. A. Abramowicz, A model of a thick disk with equatorial accretion, *Astrophys. J.* **253**, 897 (1982).
  - [11] R. Narayan, A. Sądowski, R. F. Penna, and A. K. Kulkarni, Grmhd simulations of magnetized advection-dominated accretion on a non-spinning black hole: role of outflows: Magnetized advection-dominated accretion, *Monthly Notices of the Royal Astronomical Society* **426**, 3241–3259 (2012).
  - [12] I. V. Igumenshchev, R. Narayan, and M. A. Abramowicz, Three-dimensional Magnetohydrodynamic Simulations of Radiatively Inefficient Accretion Flows, *Astrophys. J.* **592**, 1042 (2003), arXiv:astro-ph/0301402 [astro-ph].
  - [13] J. C. McKinney, A. Tchekhovskoy, and R. D. Blandford, General relativistic magnetohydrodynamic simulations of magnetically choked accretion flows around black holes, *Monthly Notices of the Royal Astronomical Society* **423**, 3083 (2012), <https://academic.oup.com/mnras/article-pdf/423/4/3083/17334055/mnras0423-3083.pdf>.
  - [14] L. Rezzolla, O. Zanotti, and J. A. Font, Dynamics of thick discs around Schwarzschild-de Sitter black holes, *Astronomy and Astrophysics* **412**, 603 (2003), arXiv:gr-qc/0310045 [gr-qc].

- [15] Z. Stuchlík, P. Slaný, and J. Kovář, Pseudo-newtonian and general relativistic barotropic tori in schwarzschild–de sitter spacetimes, *Classical and Quantum Gravity* **26**, 215013 (2009).
- [16] S. Chakraborty, Equilibrium configuration of perfect fluid orbiting around black holes in some classes of alternative gravity theories, *Classical and Quantum Gravity* **32**, 075007 (2015).
- [17] P. I. Jefremov, Circular motion and Polish Doughnuts in NUT spacetime, in *New Frontiers in Black Hole Astrophysics*, Vol. 324, edited by A. Gomboc (2017) pp. 353–354.
- [18] M. C. Teodoro, L. G. Collodel, D. Doneva, J. Kunz, P. Nedkova, and S. Yazadjiev, Polish doughnuts around scalarized kerr black holes (2021), arXiv:2108.08640 [gr-qc].
- [19] M. C. Teodoro, L. G. Collodel, and J. Kunz, Retrograde polish doughnuts around boson stars, *Journal of Cosmology and Astroparticle Physics* **2021** (03), 063.
- [20] S. Bahamonde, S. Faraĵi, E. Hackmann, and C. Pfeifer, Thick accretion disk configurations in the born-infeld teleparallel gravity, *Phys. Rev. D* **106**, 084046 (2022).
- [21] X. Zhou, S. Chen, and J. Jing, Geometrically thick equilibrium tori around a dyonic black hole with quasi-topological electromagnetism, *European Physical Journal C* **84**, 130 (2024), arXiv:2307.01996 [gr-qc].
- [22] C. Chen, Q. Pan, and J. Jing, Geometrically thick equilibrium tori around a schwarzschild black hole in swirling universes (2024), arXiv:2402.02789 [gr-qc].
- [23] F. J. Ernst, New Formulation of the Axially Symmetric Gravitational Field Problem. II, *Phys. Rev.* **168**, 1415 (1968).
- [24] F. J. Ernst, New formulation of the axially symmetric gravitational field problem, *Phys. Rev.* **167**, 1175 (1968).
- [25] J. Barrientos, A. Cisterna, I. Kolář, K. Müller, M. Oyarzo, and K. Pallikaris, Mixing "Magnetic" and "Electric" Ehlers–Harrison transformations: The Electromagnetic Swirling Spacetime and Novel Type I Backgrounds, (2024), arXiv:2401.02924 [gr-qc].
- [26] G. W. Gibbons, A. H. Mujtaba, and C. N. Pope, Ergoregions in Magnetised Black Hole Spacetimes, *Class. Quant. Grav.* **30**, 125008 (2013), arXiv:1301.3927 [gr-qc].
- [27] M. Astorino, R. Martelli, and A. Viganò, Black holes in a swirling universe, *Phys. Rev. D* **106**, 064014 (2022), arXiv:2205.13548 [gr-qc].
- [28] F. J. Ernst, Black holes in a magnetic universe, *J. Math. Phys.* **17**, 54 (1976).
- [29] R. Capobianco, B. Hartmann, and J. Kunz, Geodesic Motion in a Swirling Universe: The complete set of solutions, (2023), arXiv:2312.17347 [gr-qc].
- [30] L. Smarr, Surface Geometry of Charged Rotating Black Holes, *Phys. Rev. D* **7**, 289 (1973).
- [31] B. Kleihaus, J. Kunz, S. Mojica, and E. Radu, Spinning black holes in Einstein–Gauss-Bonnet–dilaton theory: Nonperturbative solutions, *Phys. Rev. D* **93**, 044047 (2016), arXiv:1511.05513 [gr-qc].